

Quantitative scanning thermal microscopy of ErAs/GaAs superlattice structures grown by molecular beam epitaxy

K. W. Park, H. P. Nair, A. M. Crook, S. R. Bank, and E. T. Yu

Citation: *Appl. Phys. Lett.* **102**, 061912 (2013); doi: 10.1063/1.4792757

View online: <http://dx.doi.org/10.1063/1.4792757>

View Table of Contents: <http://apl.aip.org/resource/1/APPLAB/v102/i6>

Published by the [American Institute of Physics](http://www.aip.org).

Related Articles

Fabrication of nanopores in 1nm thick carbon nanomembranes with slow highly charged ions
Appl. Phys. Lett. **102**, 063112 (2013)

High pressure phase transition of ZnO/SiO₂ core/shell nanospheres
J. Appl. Phys. **113**, 054314 (2013)

Nonlinear bleaching, absorption, and scattering of 532-nm-irradiated plasmonic nanoparticles
J. Appl. Phys. **113**, 053107 (2013)

Optimal conditions for magnetization reversal of nanocluster assemblies with random properties
J. Appl. Phys. **113**, 043902 (2013)

Surface plasmon enhanced photoluminescence and Raman scattering of ultra thin ZnO-Au hybrid nanoparticles
J. Appl. Phys. **113**, 033512 (2013)

Additional information on *Appl. Phys. Lett.*

Journal Homepage: <http://apl.aip.org/>

Journal Information: http://apl.aip.org/about/about_the_journal

Top downloads: http://apl.aip.org/features/most_downloaded

Information for Authors: <http://apl.aip.org/authors>

ADVERTISEMENT

AIP | Applied Physics
Letters

SURFACES AND INTERFACES
Focusing on physical, chemical, biological, structural, optical, magnetic and electrical properties of surfaces and interfaces, and more...

ENERGY CONVERSION AND STORAGE
Focusing on all aspects of static and dynamic energy conversion, energy storage, photovoltaics, solar fuels, batteries, capacitors, thermoelectrics, and more...

EXPLORE WHAT'S NEW IN APL

SUBMIT YOUR PAPER NOW!

Quantitative scanning thermal microscopy of ErAs/GaAs superlattice structures grown by molecular beam epitaxy

K. W. Park, H. P. Nair, A. M. Crook, S. R. Bank, and E. T. Yu^{a)}

Microelectronics Research Center, University of Texas at Austin, 10100 Burnet Rd., Austin, Texas 78758, USA

(Received 18 December 2012; accepted 6 February 2013; published online 15 February 2013)

A proximal probe-based quantitative measurement of thermal conductivity with ~ 100 – 150 nm lateral and vertical spatial resolution has been implemented. Measurements on an ErAs/GaAs superlattice structure grown by molecular beam epitaxy with 3% volumetric ErAs content yielded thermal conductivity at room temperature of 9 ± 2 W/m K, approximately five times lower than that for GaAs. Numerical modeling of phonon scattering by ErAs nanoparticles yielded thermal conductivities in reasonable agreement with those measured experimentally and provides insight into the potential influence of nanoparticle shape on phonon scattering. Measurements of wedge-shaped samples created by focused ion beam milling provide direct confirmation of depth resolution achieved. © 2013 American Institute of Physics. [<http://dx.doi.org/10.1063/1.4792757>]

Incorporation of nanoparticles or other nanostructures in crystalline semiconductor materials is emerging as a highly effective approach for engineering thermal transport behavior, as the resulting increase in phonon scattering can lead to large reductions in thermal conductivity that are desirable for thermoelectric device applications.^{1–5} Furthermore, the presence of such structures within other types of semiconductor devices may be expected to influence thermal transport and consequently thermal management strategies in those devices.^{1,2} In this context, III-V semiconductor/rare earth-V nanocomposite materials are of particular interest due to the potential for epitaxial incorporation of rare earth-V nanoparticles in a single-crystal III-V semiconductor to reduce thermal conductivity, and interest in such nanocomposite materials encompasses a variety of device applications including multijunction solar cells,⁶ high-speed modulators,⁷ thermoelectrics,^{1–3} and fast photoconductors for THz sources and receivers.^{8–10} However, methods for quantitative assessment of thermal transport behavior at the nanoscale remain challenging.

In this letter, we report studies in which the 3ω technique for measuring thermal conductivity^{11–13} was implemented using a functionalized probe in an atomic force microscope^{14–19} and used to obtain quantitative measurements of thermal conductivity in an ErAs/GaAs superlattice structure grown by molecular beam epitaxy. This approach allows us to achieve very high spatial resolution in measuring thermal conductivity of ~ 100 nm laterally and ~ 150 nm in depth, limited by the size of the probe tip apex. With calibration using materials of known thermal conductivity, quantitative accuracy of approximately $\pm 20\%$ was achieved over the range of thermal conductivities of interest in this work. We find that incorporation of ErAs nanoparticles with even a low ($\sim 3\%$) average concentration of ErAs leads to a reduction in room-temperature thermal conductivity by approximately a factor of five, from ~ 50 W/m K in GaAs to 9 ± 2 W/m K in the ErAs/GaAs superlattice, and show that this result is in reasonable accord with numerical

modeling of phonon scattering by ErAs nanoparticles embedded in GaAs.

The ErAs/GaAs superlattice structure employed in this work was grown by solid-source molecular beam epitaxy (MBE) in a Varian Gen II system. The sample structure consisted of a 150 nm undoped GaAs buffer layer grown at 580 °C on a semi-insulating GaAs (001) substrate, followed by a 200 nm ErAs/GaAs superlattice consisting of 40 repetitions of 0.5 monolayer (ML) ErAs and 5 nm GaAs grown at 450 °C. Under these growth conditions, the ErAs layers form 3–4 ML (~ 0.9 – 1.1 nm) high nanoparticles with diameters of ~ 3 nm, leading to an average fill factor of 0.14 for each ErAs layer and allowing high-quality overgrowth of the ErAs nanoparticle seeded by the exposed GaAs remaining after deposition of each ErAs layer.²⁰

Scanning thermal microscopy measurements were performed under ambient conditions using a Bruker Dimension ICON scanning probe microscopy system equipped with a functionalized probe in which a thin patterned Pd film on the probe tip served as a localized heater and thermometer. In a manner analogous to the standard 3ω measurement in a planar geometry,^{11–13} an electrical excitation signal at frequency ω induces variations in the resistance of the functionalized probe tip, corresponding to changes in its temperature, at frequency 3ω that are detected using a Wheatstone bridge circuit configuration and lock-in amplifier. The measurement apparatus and experimental geometry are shown schematically in Fig. 1(a). The functionalized probe was connected to one arm of the Wheatstone bridge circuit that also included two resistors, R_1 and R_2 , of known value and one variable resistor used to balance the bridge. The functionalized probe tip, shown in Fig. 1(b), incorporated a Pd thin-film resistor, deposited on SiO₂, which served as a heater and thermometer. An input voltage signal at frequency ω was used to excite the bridge circuit, and the 3ω frequency component of the voltage difference between opposite nodes, $V_p - V_r$, was detected by a lock-in amplifier and used to monitor the thermal behavior of the probe tip. By modeling the thermal transport between the probe tip apex and the sample, it was possible to extract information about the sample thermal conductivity. Quantitative

^{a)}Electronic mail: ety@ece.utexas.edu.

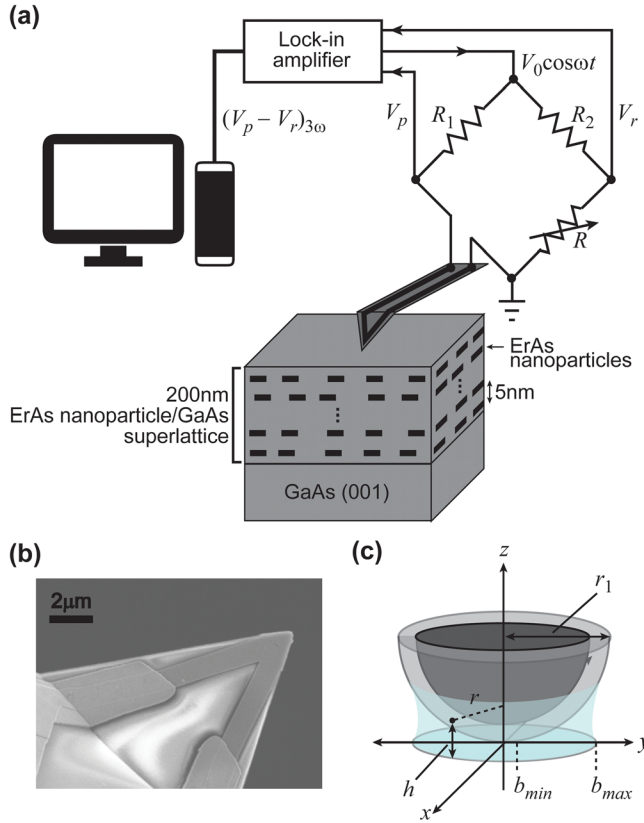


FIG. 1. (a) Schematic diagram of the ErAs/GaAs superlattice sample structure, functionalized probe tip, and electronic circuitry and signals required to perform scanned probe 3ω measurement of thermal conductivity. (b) Scanning electron micrograph of atomic force microscope probe tip functionalized with Pd thin-film resistor that serves as a local heater and thermometer. (c) Schematic diagram of probe tip and ambient water meniscus geometry used to model thermal transport between tip and sample.

determination of sample thermal conductivity was achieved via a calibration process in which (i) samples of known thermal conductivity, e.g., GaAs, Si, and SiO₂, were measured along with the actual sample of interest; (ii) the 3ω component of voltage response was modeled as a function of sample thermal conductivity; (iii) the model was calibrated to data obtained for the samples of known thermal conductivity; (iv) the unknown sample thermal conductivity was obtained from its measured 3ω response and the model calibrated to samples of known thermal conductivity.

We have adapted a thermal model employed in previous work on scanning thermal microscopy^{14,18} to determine the thermal conductivity in our samples. In this approach, the probe tip was modeled using the transient fin equation to determine the probe tip temperature and equivalent thermal contact resistance, R_{eq} , between the probe tip and sample. Heat transfer between the probe tip and sample can occur via solid-solid conduction, conduction through the liquid meniscus that forms between the probe tip and sample, and conduction through the air gap surrounding the tip-sample junction.^{21,22} The liquid meniscus is formed under ambient measurement conditions by water molecules absorbed on the sample and tip surfaces. We modeled R_{eq} by including two thermal resistance components in parallel—the electroconstriction resistance associated with the solid-solid contact between probe tip and sample surface, R_c , and the thermal resistance associated with the water meniscus, R_m .

Depending on the relative magnitudes of the solid-solid contact radius, r_c , and phonon mean free path, λ_{ph} , the electroconstriction resistance may include various combinations of diffusive (for $r_c \gg \lambda_{ph}$) and ballistic (for $r_c \ll \lambda_{ph}$) components; it has been shown that the sum of these two components provides a good approximation to obtain the total electroconstriction resistance.²³ We used the diffuse mismatch model^{23,24} to calculate the ballistic resistance component for two adjoining solid materials, and the estimated ballistic component was two orders of magnitude smaller than the diffusive component so the diffusive component dominates in our work. R_c is then computed by modeling the tip-sample contact as a sphere in contact with a flat surface, as shown schematically in Fig. 1(c), for which the thermal resistance is given by²³

$$R_c = \frac{1}{4r_c} \left(\frac{1}{\kappa_p} + \frac{1}{\kappa_s} \right), \quad (1)$$

where κ_p and κ_s are the thermal conductivities of the probe tip and sample, respectively. R_m is computed assuming the same geometry for the probe tip and sample and is given by^{23,25}

$$\frac{1}{R_m} = \frac{1}{\Delta T_{\max}} \int_{b_{\min}}^{b_{\max}} \kappa_m \frac{\Delta T(r)}{h(r)} 2\pi r dr$$

$$= 2\pi\kappa_m \left[\sqrt{r_1^2 - r^2} + r_1 \log \left(\sqrt{r_1^2 - r^2} - r_1 \right) \right]_{b_{\min}}^{b_{\max}}, \quad (2)$$

where κ_m is the thermal conductivity of the water forming the meniscus and r_1 , b_{\min} , and b_{\max} are the tip radius, minimum-, and maximum radii of the water meniscus, as shown in Fig. 1(c). $\Delta T(r)$ is the position dependent temperature difference between the thermal probe and substrate, which assumes a maximum values ΔT_{\max} . In our calculations, we assume the probe is isothermal in the immediate vicinity the tip apex, so that $\Delta T(r) = \Delta T_{\max}$.²⁵ R_{eq} is then given by

$$R_{eq} = \frac{R_c R_m}{R_c + R_m}. \quad (3)$$

Experimental measurement of the 3ω frequency component of $V_p - V_r$, as shown in Fig. 1(a), yields the temperature of the probe tip, from which the sample thermal conductivity can be determined using the model described above. For modeling of the amplitude and phase of $V_{3\omega}$, we also account for the NiCr current limiters integrated into the thermal probe tip using a first order low-pass filter function.¹⁸

To provide the calibration necessary to obtain a quantitative measurement of thermal conductivity for the ErAs/GaAs superlattice, multiple measurements were performed on each of the following five samples: (i) 15 μm of SiO₂ formed by thermal oxidation; (ii) a GaAs (001) undoped wafer; (iii) a crystalline Si (001) n-type wafer; (iv) a silicon-on-insulator (SOI) wafer with Si layer thickness of 1000 nm and oxide thickness of 1000 nm; and (v) the ErAs/GaAs superlattice sample. Prior to measurement, all samples were cleaned with acetone and isopropyl alcohol followed by a dry

nitrogen spray. Figure 2(a) shows $(V_p - V_r)_{3\omega} \equiv V_{3\omega}$ measured as a function of frequency and with an excitation amplitude $V_0 = 0.65$ V for all samples. Small, but clearly discernible, differences are evident among the samples measured, as made evident by the magnified vertical axis employed in the signal range corresponding to frequencies of 100 Hz and below. Figure 2(b) shows the measured and modeled amplitude and phase of $V_{3\omega}$ as functions of frequency for the crystalline Si sample. A comparison of Figs. 2(a) and 2(b) shows that all samples exhibit the same characteristic dependence of $V_{3\omega}$ on frequency, and in Fig. 2(b) the comparison of experimental and modeled signal amplitude confirms the excellent agreement, over all measured frequencies, between the measured and modeled signal values. Fig. 2(c) shows the amplitude of $V_{3\omega}$ at 50 Hz modeled as a function of sample thermal conductivity, along with the measured signal values for the five materials characterized. The vertical error bars in Fig. 2(c) correspond to multiple measurements performed for each material. For SiO_2 , GaAs,

Si, and SOI, the sample thermal conductivities were assumed to correspond to their established values (hence the absence of horizontal error bars), and agreement between the numerical model and experimental measurements was excellent. This enabled us to use the measured amplitude of $V_{3\omega}$ for the ErAs/GaAs superlattice structure, combined with the numerical model, to obtain the superlattice thermal conductivity value of 9 ± 2 W/m K indicated in the Fig. 2(c). The uncertainty given for this value of the superlattice thermal conductivity was obtained by taking the statistical uncertainty in the measured values of $V_{3\omega}$ for that sample and fitting the upper and lower end of the statistical range to the thermal model.

To understand the influence of phonon scattering by ErAs nanoparticles on the ErAs/GaAs superlattice thermal conductivity, we have also performed theoretical estimates of the relevant scattering processes using the Callaway model.^{26–28} At room temperature, it is anticipated that the Umklapp and mass difference scattering processes are dominant rather than normal scattering process.^{26,27} The combined phonon relaxation time τ_c is given, using Matthiessen's rule, by

$$\tau_c^{-1} = \tau_U^{-1} + \tau_M^{-1} + \tau_{e-ph}^{-1} + \tau_{np}^{-1}, \quad (4)$$

where τ_U , τ_M , τ_{e-ph} , and τ_{np} are, respectively, relaxation times associated with Umklapp, mass difference (isotopes), electron-phonon, and ErAs nanoparticle scattering.^{2,29,30} τ_U , τ_M , and τ_{e-ph} are computed using established parameters from the literature.^{27,31–33} τ_{np} is computed by first calculating the nanoparticle scattering cross section as a function of phonon frequency and nanoparticle size, assuming a spherical nanoparticle shape, and then computing the relaxation time from the nanoparticle density, phonon group velocity, and scattering cross section averaged over the expected nanoparticle size distribution.^{29,30} We have also attempted to account, at least approximately, for varying shapes of the ErAs nanoparticles in the computation of phonon scattering. For the growth conditions employed here, the ErAs is expected to form nanoparticles ~ 1.5 nm in radius and 3–4 ML (~ 1 nm) high, leading to a disk-like shape.²⁰ To account for this shape in the model, we assume that phonon scattering scales with the nanoparticle cross-sectional area projected onto the plane normal to the phonon wave vector; for a phonon whose wave vector is at an angle θ to the (001) nanoparticle surface, this yields factor of $\cos(\theta)$ in the scattering cross section with an additional correction for the disk thickness. An effective scattering cross-section was then calculated by averaging over angles ranging from 0° to 90° . For the expected ErAs average nanoparticle radius of 1.5 nm with a standard deviation of 1 nm and ErAs content of 3%, this model yields a thermal conductivity of ~ 15 W/m K, reasonably close to the experimentally measured value given the approximate nature of the model, uncertainties in the model parameters, and lack of free parameters.

Finally, to assess the depth sensitivity of the proximal probe 3ω measurement and verify that these measurements were sensitive to the thermal transport properties of only the superlattice structure and not the underlying GaAs buffer layer and substrate, a wedge-shaped sample structure was prepared using focused ion beam (FIB) milling, as shown schematically in Fig. 3(a). A gallium ion beam at 30 keV

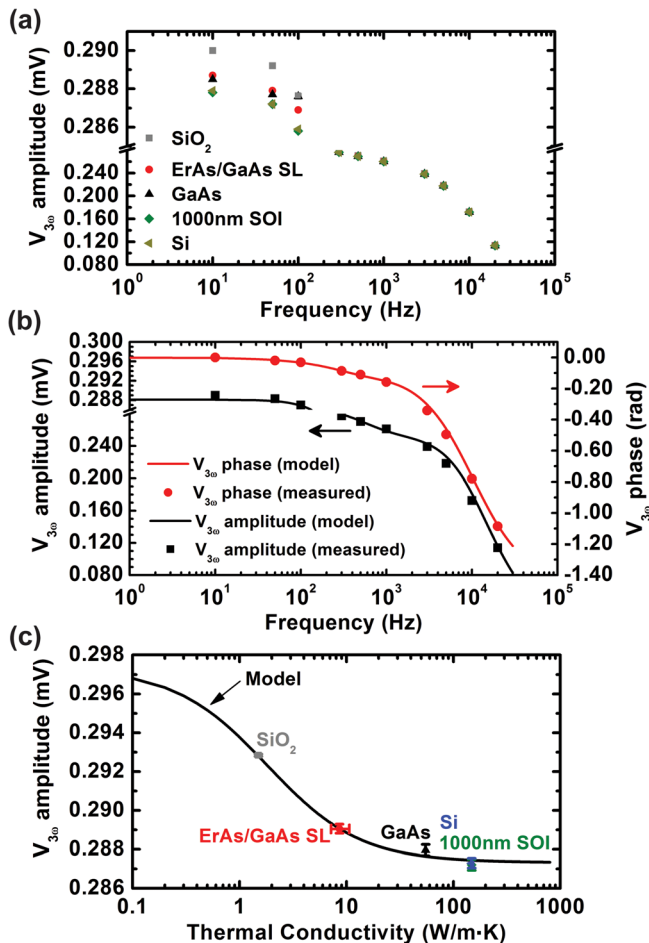


FIG. 2. (a) $V_{3\omega}$ signal amplitude measured as function of frequency for SiO_2 , ErAs/GaAs superlattice structure, GaAs, Si, and 1000 nm SOI. (b) Measured (symbols) and numerically modeled (lines) $V_{3\omega}$ signal amplitude and phase for Si sample, confirming excellent agreement between modeled and measured frequency dependence of $V_{3\omega}$. (c) $V_{3\omega}$ signal amplitude predicted by numerical modeling (solid line) and measured at 50 Hz for SiO_2 , ErAs/GaAs superlattice structure, GaAs, Si, and 1000 nm SOI. For all materials except the ErAs/GaAs superlattice, the thermal conductivity is assumed to be known, enabling calibration of the numerical model. The thermal conductivity of the ErAs/GaAs superlattice structure is then determined from its measured $V_{3\omega}$ signal amplitude and the numerical model.

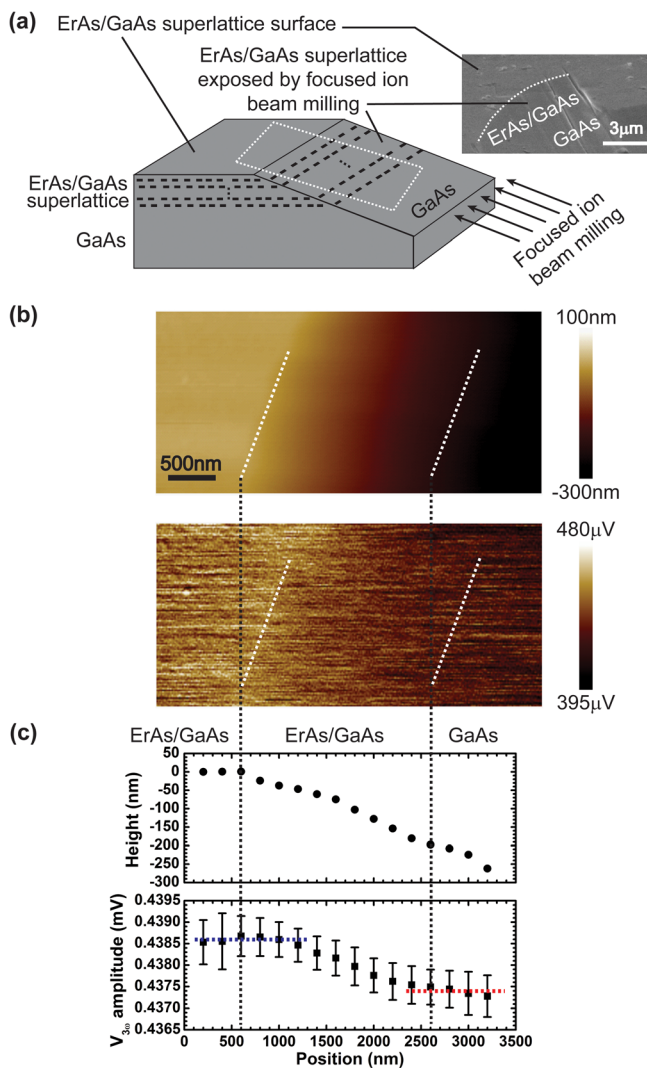


FIG. 3. (a) Schematic diagram and scanning electron micrograph of focused-ion-beam milled wedge sample structure showing the milling geometry and cross-sectional ramp to expose the ErAs/GaAs superlattice and underlying GaAs; the approximate location of images in (b) is indicated by the white dotted line. (b) Atomic force topograph and 3ω signal image, obtained simultaneously, of wedge structure across surface region with ErAs/GaAs superlattice thickness varying from 200 nm to 0 nm. White dotted lines indicate regions from which plots in (c) were extracted. (c) Plots of surface height and 3ω signal amplitude showing that 3ω signal is constant (blue dotted line, corresponding to constant sample thermal conductivity) for ErAs/GaAs superlattice thicknesses of ~ 150 – 200 nm, then decreased gradually for reduced superlattice thicknesses, due to the increased contribution to the thermal conductivity of the GaAs substrate, eventually reaching a value corresponding to the thermal conductivity of the GaAs buffer layer and substrate (red dotted line). Each data point represents an average and, for $V_{3\omega}$ amplitude, standard deviation indicated by error bars, along a 1500 nm line parallel to the white dotted lines shown in (b).

was used to expose a cross-section of the ErAs/GaAs superlattice and underlying GaAs layers at an angle of $\sim 6^\circ$, producing a wedge structure in which the ErAs/GaAs superlattice thickness at the sample surface varied continuously from 200 nm to 0 nm over a lateral distance of 2000 nm. Figure 3(b) shows an atomic force micrograph and 3ω signal image at a fundamental frequency of 850 Hz, obtained simultaneously, for an area encompassing the unetched ErAs/GaAs superlattice surface and cross sections of the ErAs/GaAs superlattice and underlying GaAs exposed by FIB milling, as indicated schematically by the white

dotted line in Fig. 3(a). Figure 3(c) shows plots of topographic height and 3ω voltage signal extracted from the images in Fig. 3(b) along a direction parallel to, and within the area bounded by, the white dotted lines indicated in the images. The regions corresponding to the ErAs/GaAs superlattice (001) surface and the exposed cross-sections of the superlattice and underlying GaAs are indicated. Each point shown in Fig. 3(c) represents the signal value averaged along a 1500 nm line parallel to the white dotted lines shown in Fig. 3(b). The error bars shown for $V_{3\omega}$ amplitude in Fig. 3(c) are associated with the signal variations measured along each such line during sample scanning; however, the average values shown clearly reveal the trend in thermal response as a function of location along the wedge profile. As can be seen in Fig. 3(c), the measured 3ω signal and therefore the sample thermal conductivity remained constant for the ErAs/GaAs superlattice (001) surface and the superlattice cross-section until the superlattice thickness directly beneath the tip was reduced to ~ 150 nm. The measured 3ω signal then decreased steadily, corresponding to increasing thermal conductivity, due to decreasing superlattice thickness, reaching an approximately constant value with the probe tip over the GaAs surface or an ErAs/GaAs superlattice thickness of ~ 20 nm or less. The difference in signal values between those shown in Figs. 2 and 3 arises due to the use of a higher excitation amplitude ($V_0 = 0.69$ V), different measurement frequency, and different probe tip. These factors affect the magnitude of the signal level observed, but in a manner that can be accounted for in detail using the thermal measurement model described above.

Observation of a constant 3ω signal for ErAs/GaAs superlattice thicknesses of 150–200 nm suggests that the proximal probe 3ω measurement achieves a depth resolution of approximately 150 nm. For lower ErAs/GaAs superlattice thicknesses, the measurement probes the combined thermal transport properties of the ErAs/GaAs superlattice and underlying GaAs, eventually being dominated by the higher thermal conductivity of the GaAs for very small superlattice thicknesses or when the superlattice is completely absent. The high spatial resolution, both laterally and in depth, afforded by this technique can be particularly advantageous in characterization of thin film materials and nanostructures in which variation in thermal behavior at these length scale are present.

In summary, we have used a 3ω thermal conductivity measurement implemented in a scanning probe microscope to characterize thermal conductivity in an ErAs/GaAs superlattice. By performing detailed numerical modeling of thermal transport at and near the probe tip-sample interface and calibrating measured signals using samples of known thermal conductivity, we are able to perform quantitative measurements of thermal conductivity in unknown samples with lateral and depth resolution of ~ 100 – 150 nm. We obtained a value of 9 ± 2 W/m K for thermal conductivity at room temperature in an ErAs/GaAs superlattice with $\sim 3\%$ average ErAs content, approximately 5 times lower than that for GaAs. Numerical modeling of phonon scattering by ErAs nanoparticles yielded values for thermal conductivity in good agreement with those measured experimentally. The level of spatial resolution we demonstrate is much higher than that attainable in 3ω measurements performed using

more conventional geometries and is anticipated to enable future studies of thermal conductivity at nanoscale dimensions in a variety of solid-state nanostructures.

This work was supported by ARO through the PECASE Program (W911NF-09-1-0434) monitored by Dr. Dwight Woolard, ONR through the YIP (N00014-10-1-0763) monitored by Dr. Dan Green, the National Science Foundation (DMR 1066430), and the Judson S. Swearingen Regents Chair in Engineering at the University of Texas at Austin.

- ¹J. M. Zide, D. O. Klenov, S. Stemmer, A. C. Gossard, G. Zeng, J. E. Bowers, D. Vashaee, and A. Shakouri, *Appl. Phys. Lett.* **87**, 112102 (2005).
- ²W. Kim, J. M. Zide, A. Gossard, D. O. Klenov, S. Stemmer, A. Shakouri, and A. Majumdar, *Phys. Rev. Lett.* **96**, 045901 (2006).
- ³G. Zeng, J. E. Bowers, J. M. O. Zide, A. C. Gossard, W. Kim, S. Singer, A. Majumdar, R. Singh, Z. Bian, Y. Zhang, and A. Shakouri, *Appl. Phys. Lett.* **88**, 113502 (2006).
- ⁴N. Mingo, D. Hauser, N. P. Kobayashi, M. Plissonnier, and A. Shakouri, *Nano Lett.* **9**, 711 (2009).
- ⁵W. Kim, S. L. Singer, A. Majumdar, D. Vashaee, Z. X. Bian, A. Shakouri, G. Zeng, J. E. Bowers, J. M. O. Zide, and A. C. Gossard, *Appl. Phys. Lett.* **88**, 242107 (2006).
- ⁶J. M. O. Zide, A. Kleiman-Shwarscstein, N. C. Strandwitz, J. D. Zimmerman, T. Steenblock-Smith, A. C. Gossard, A. Forman, A. Ivanovskaya, and G. D. Stucky, *Appl. Phys. Lett.* **88**, 162103 (2006).
- ⁷H. Chen, W. J. Padilla, J. M. O. Zide, S. R. Bank, A. C. Gossard, A. J. Taylor, and R. D. Averitt, *Opt. Lett.* **32**, 1620 (2007).
- ⁸C. Kadow, S. B. Fleischer, J. P. Ibbetson, J. E. Bowers, A. C. Gossard, J. W. Dong, and C. J. Palmstrom, *Appl. Phys. Lett.* **75**, 3548 (1999).
- ⁹J. E. Bjarnason, T. L. J. Chan, A. W. M. Lee, E. R. Brown, D. C. Driscoll, M. Hanson, A. C. Gossard, and R. E. Muller, *Appl. Phys. Lett.* **85**, 3983 (2004).
- ¹⁰J. F. O'Hara, J. M. O. Zide, A. C. Gossard, A. J. Taylor, and R. D. Averitt, *Appl. Phys. Lett.* **88**, 251119 (2006).
- ¹¹D. G. Cahill, *Rev. Sci. Instrum.* **61**, 802 (1990).
- ¹²D. G. Cahill and R. O. Pohl, *Phys. Rev. B* **35**, 4067 (1987).
- ¹³N. O. Birge, *Phys. Rev. B* **34**, 1631 (1986).
- ¹⁴S. Lefèvre and S. Volz, *Rev. Sci. Instrum.* **76**, 033701 (2005).
- ¹⁵S. Lefèvre, J.-B. Saulnier, C. Fuentes, and S. Volz, *Superlattices Microstruct.* **35**, 283 (2004).
- ¹⁶M. Chirtoc, J. Gibkes, R. Wernhardt, J. Pelzl, and A. Wieck, *Rev. Sci. Instrum.* **79**, 093703 (2008).
- ¹⁷E. Puyoo, S. Grauby, J.-M. Rampnoux, E. Rouvière, and S. Dilhaire, *Rev. Sci. Instrum.* **81**, 073701 (2010).
- ¹⁸E. Puyoo, S. Grauby, J.-M. Rampnoux, E. Rouvière, and S. Dilhaire, *J. Appl. Phys.* **109**, 024302 (2011).
- ¹⁹J. Bodzenta, A. Kaźmierczak-Bałata, M. Lorenc, and J. Juszczyk, *Int. J. Thermophys.* **31**, 150 (2010).
- ²⁰C. Kadow, J. A. Johnson, K. Kolstad, J. P. Ibbetson, and A. C. Gossard, *J. Vac. Sci. Technol. B* **18**, 2197 (2000).
- ²¹L. Shi and A. Majumdar, *J. Heat Transfer* **124**, 329 (2002).
- ²²L. Shi, S. Plyasunov, A. Bachtold, P. L. McEuen, and A. Majumdar, *Appl. Phys. Lett.* **77**, 4295 (2000).
- ²³R. Prasher, *Nano Lett.* **5**, 2155 (2005).
- ²⁴G. Chen, *Nanoscale Energy Transport and Conversion* (Oxford University Press, 2005).
- ²⁵V. Bahadur, J. Xu, Y. Liu, and T. S. Fisher, *J. Heat Transfer* **127**, 664 (2005).
- ²⁶A. Balandin and K. L. Wang, *Phys. Rev. B* **58**, 1544 (1998).
- ²⁷J. Zou and A. Balandin, *J. Appl. Phys.* **89**, 2932 (2001).
- ²⁸J. Callaway, *Phys. Rev.* **113**, 1046 (1959).
- ²⁹W. Kim, S. L. Singer, A. Majumdar, J. M. O. Zide, D. Klenov, A. C. Gossard, and S. Stemmer, *Nano Lett.* **8**, 2097 (2008).
- ³⁰W. Kim and A. Majumdar, *J. Appl. Phys.* **99**, 084306 (2006).
- ³¹R. Y. Wang, R. A. Segalman, and A. Majumdar, *Appl. Phys. Lett.* **89**, 173113 (2006).
- ³²J. S. Blakemore, *J. Appl. Phys.* **53**, R123 (1982).
- ³³S. Adachi, *GaAs and Related Materials: Bulk Semiconducting and Superlattice Properties* (World Scientific, 1994).